Supplementary Information

Interface catalytic regulation *via* the electron rearrangement and hydroxyl radicals triggered by oxygen vacancies and heavy metal ions

Xiang-Yu Xiao,[a,b] Zong-Yin Song,[a,b] Chong-Chong Zhang,[c] Yong-Huan Zhao,[a,b] Zhi-Wei Gao,[a,b] Shi-Hua Chen,[a] Pei-Hua Li,[a] Yu-Feng Sun,[c] Meng Yang,[a,*] Xing-Jiu Huang [a,b,*]

[a] Key Laboratory of Environmental Optics and Technology, And Environmental Materials and Pollution Control Laboratory, Institute of Solid State Physics, HFIPS, Chinese Academy of Sciences, Hefei 230031, P. R. China

[b] Department of Materials Science and Engineering, University of Science and Technology of China, Hefei 230026, P. R. China

[c] College of Mechanical and Automotive Engineering, Anhui Polytechnic University, Wuhu, Anhui 241000, PR China

*Corresponding author

Email addresses: myang@iim.ac.cn; xingjiuhuang@iim.ac.cn

Table of contents

3. Tables

4. References

1. Experimental Section

1.1. Characterization. The morphology of the ZrO_2 hollow sphere is examined by Focused Ion beam (FIB) (AURIGA, ZEISS Co) and high-resolution transmission electron microscopy (HRTEM; JEM-2010, JEOL Co). Thermochromic ESCALab 250 Xi with a monochromatic Al Kα X-ray source was used to analyze the chemical composition of ZrO_2 under a 500 μm beam spot with a fixed dialysis energy of 30 eV. Shimadzu UV-3600 instrument was used to measure the UV-Vis diffuse reflectance spectrum of the sample in the range of 200-1000 nm, and $BaSO_4$ was used as reference. Infrared spectra were recorded by FT-IR spectrometer in the range of 4000~600 cm^{-1} (MagnaIR 750, Nicolet Instrument, USA). EPR tests were implemented with Bruker EMX plus 10/12 (equipped with Oxford ESR910 Liquid Helium cryostat). Electrochemical testing using a computer-controlled CHI 660D electrochemical workstation (Shanghai Chenhua Instrument Co).

1.2. Chemical reagents. Zirconocene dichloride (99%) was purchased from Aladdin (Shanghai, China). Acetone (AR) and other required chemicals come from Sinopharm Chemical Reagent Co., Ltd. (China). 5,5- Dimethyl-1-oxaporphyrin-N-oxide (DMPO) and 2,2,6,6-Tetramethyl-4- piperidine (TEMP) were obtained from Macklin Biochemical Co. Ltd. HAc-NaAc buffer solutions with different pH were prepared at different ratios of 0.1 M NaAc and 0.1 M HAc. Adjusting the different volume ratios of 0.1 M KH_2PO_4 and Na_2HPO_4 to different pH phosphate buffer solutions (PBS). Similarly, 0.1 M $NH_3{\bullet}H_2O$-

NH_4Cl solution of different pH is composed of 0.1 M NH_4Cl and $NH_3{\bullet}H_2O$. The pH of all buffer solutions was further adjusted by 0.1 M NaOH and 0.1 M HCl.

1.3. Fabrication of ZrO_2 nanomaterial modified GCE. First, the surface of the bare GCE electrode was sequentially treated with 0.3 and 0.1 μm alumina powder and the electrode was sonicated in dilute HNO_3 solution, ethanol and ultrapure water successively for 2 minutes to obtain a clean surface. After homogeneously dispersed 1 mg of our sample in 5 mL of deionized water, transfer 7 μL of the suspension onto the electrode, dried it with N_2 and waited for overnight to use.

1.4. Electrochemical experiments. Square wave anode stripping voltammetry (SWASV) was selected as the method of electrochemical experiments, and Pb(II) was detected under the optimized conditions. The deposition voltage of -1.3 V was adopted and kept running 150 s to catalytically reduce Pb(II). Then, the SWASV curve was obtained by operating potential from -1 V and 0.6 V to oxidize the deposited Pb(0). The desorption potential was set at 1.0 V for 120 s to desorb and completely remove the residual metal. The test frequency of electrochemical impedance spectroscopy (EIS) is between 1 and 10^5 Hz.

1.5. Adsorption experiments. Typically, HAc-NaAc (pH 5.0) buffer solution was mixed with 1 mM Pb(II) in a volume ratio of 9:1 to form a 10 mL solution, and then 10 mg of ZrO_2 powder was added. The preparation method of the

other group of solutions was similar. Adding 1 mL of Hg(II), Cu(II) and Cd(II) while keeping the total volume of 10 mL. Next, the mixtures were vibrated at room temperature for 24 h, then washed twice with ultrapure water, finally freeze-dried for 12 h to obtain powder for XPS measurement.

1.6. XAFS data analysis. The Zr K-edge and Pb L_3-edge XAFS spectra were collected in transmission mode and Lytel-fluorescence mode, respectively, at the BL11B beamline of Shanghai Synchrotron Radiation Facility (SSRF). Athena software was used to subtract the background signal of the pre-edge and post-edge and to normalize spectra intensity. IFEFFIT software was employed to calibrate the energy scale and to correct the background.

1.7. *In-situ* EPR experiments. In the process of in-situ EPR experiments, the electrochemical workstation is placed adjacent to the EPR apparatus. The parameters and reagents used in SWASV tests of in-situ EPR experiments are totally consistent with that in normal electrochemical experiments except 100 μL of spin-trapping agent is additional needed to drop in the buffer solution. The sampling process occurs during the last 10 seconds of electrodeposition, where 50 μL of sample is taken by pipette from the buffer solution with thoroughly stirring. After absorbing the same amount of samples into the capillary glass tubes, the EPR experiments are carried out immediately.

2. Figures

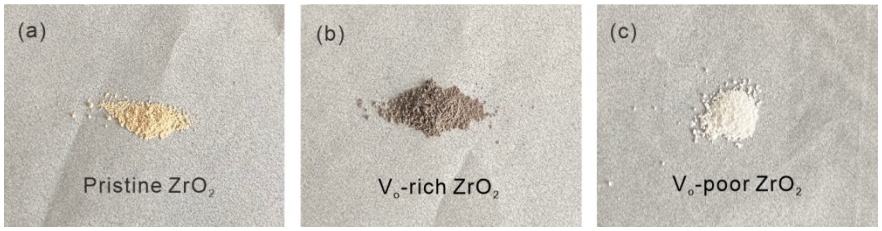

Fig. S1 The synthesized three samples of (a) pristine ZrO_2, (b) V_o-poor ZrO_2 and (c) V_o-rich ZrO_2.

The color of pristine ZrO_2, V_o-rich ZrO_2 and V_o-poor ZrO_2 are faint yellow, dark brown, and white, respectively.

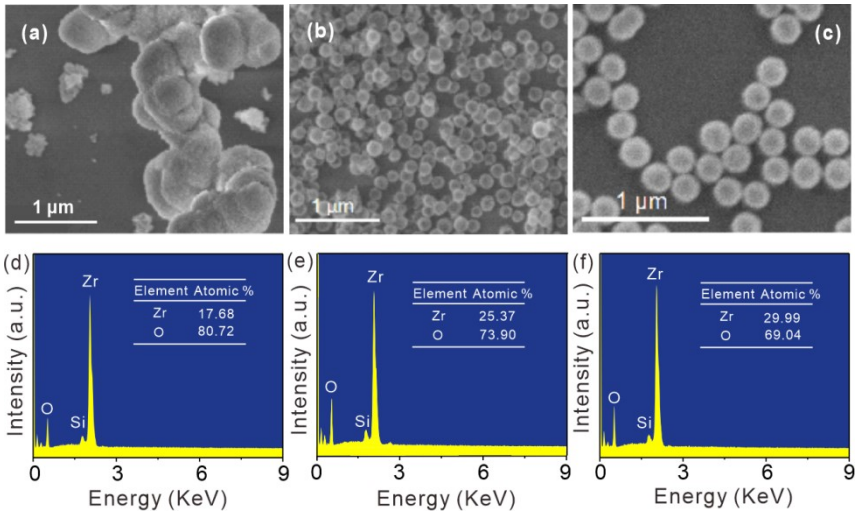

Fig. S2 The SEM images and the corresponding EDS of (a,d) V_o-poor ZrO_2, (b,e) pristine ZrO_2 and (c,f) V_o-rich ZrO_2.

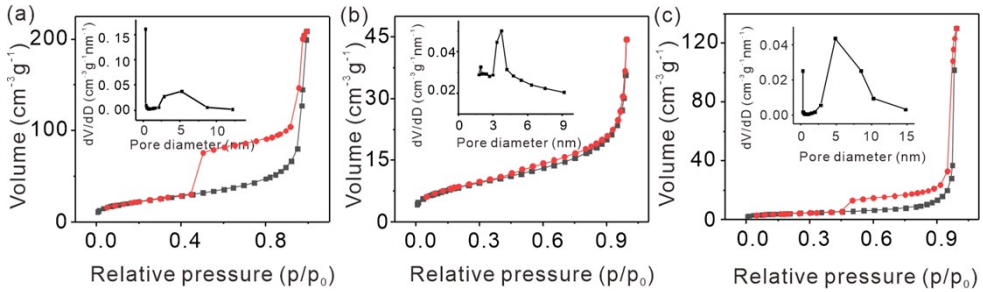

Fig. S3 N_2 adsorption–desorption isotherms and pore diameter distribution (inset) of (a) pristine ZrO_2, (b) V_o-poor ZrO_2 and (c) V_o-rich ZrO_2.

The surface areas of the pristine ZrO_2, V_o-poor ZrO_2, and V_o-rich ZrO_2 were 30 m^2/g, 14 m^2/g and 82 m^2/g, respectively, suggesting that the process of calcination cause obvious effect on the morphological structures of them. And the insertion diagrams in Fig. S3 exhibited their distribution of pore diameters were mainly between 3-10 nm.

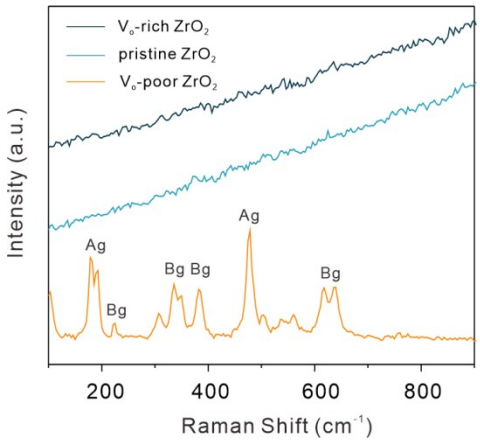

Fig. S4 The Raman spectra of pristine ZrO_2, V_o-poor ZrO_2 and V_o-rich ZrO_2.

V_o-poor ZrO_2 showed obvious peaks of Ag at 178, 191 and 476 cm^{-1}, Bg at 222, 333, 382 and 615 cm^{-1}, which were assigned to the monoclinic ZrO_2[1]. However, for pristine ZrO_2 and V_o-rich ZrO_2 (tetragonal phase), the fluorescence signals were too high to detect Raman signals due to the crystalline transition, which provided evidence that the microstructures were very different with copious oxygen vacancies in ZrO_2.

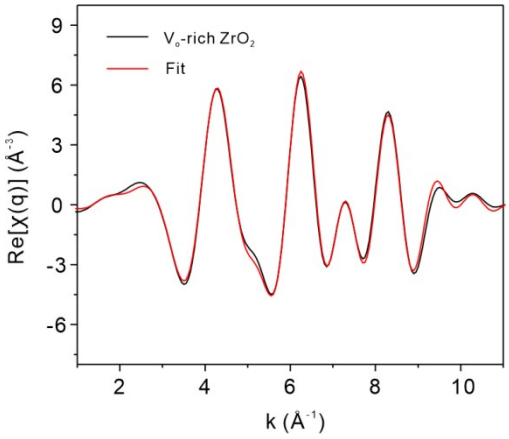

Fig. S5 The $k^3(k)$ oscillations of V_o-rich ZrO_2 corresponding to Fig. 2b.

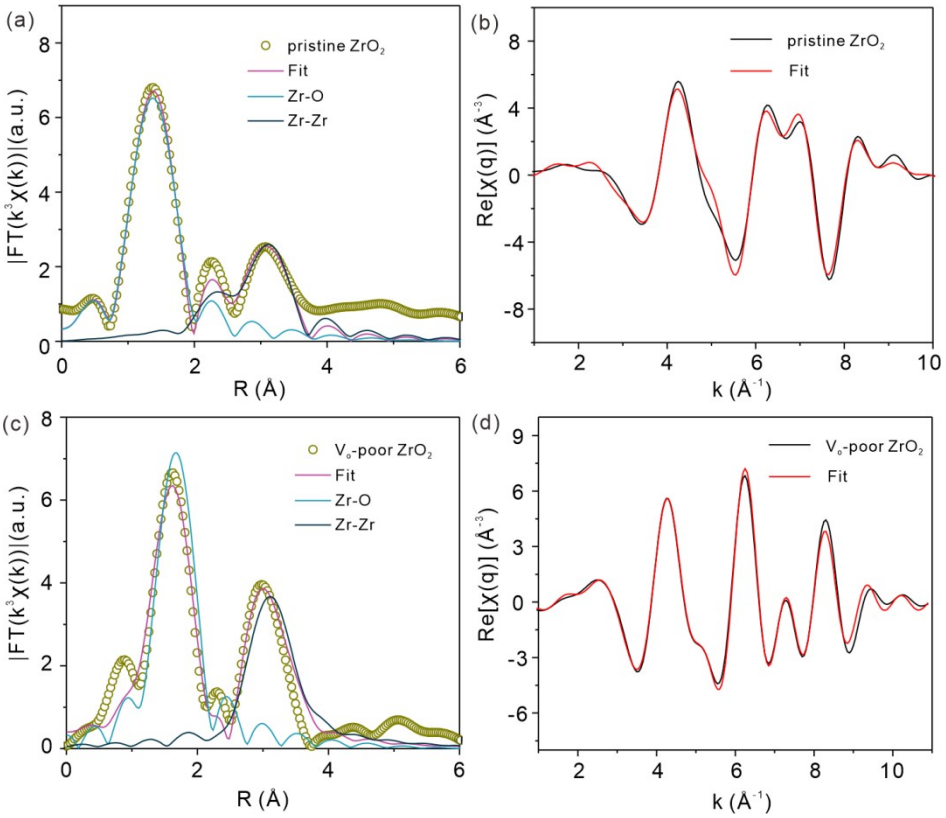

Fig. S6 The Zr K-edge EXAFS in R space (k^3-weighted) and the fitting curves of (a) pristine ZrO_2; (c) V_o-poor ZrO_2 without correcting for scattering phase shift. (b, d) The corresponding $k^3(k)$ oscillations of pristine ZrO_2; V_o-poor ZrO_2, respectively.

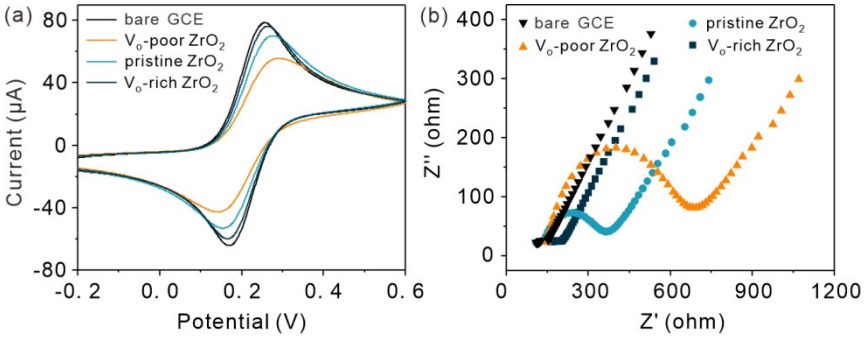

Fig. S7 (a) CV and (b) EIS spectra of the pristine ZrO_2, V_o-poor ZrO_2, and V_o-rich ZrO_2.

Obviously, the bare GCE showed the highest redox peak current due to its excellent conductivity, and V_o-rich ZrO_2 ranked the second while V_o-poor ZrO_2 had the lowest redox peak current which indicated its poor conductivity. The semicircles (Fig. S7b) represented their electron-transfer resistance (R_{et}) and the corresponding values of pristine ZrO_2, V_o-poor ZrO_2, and V_o-rich ZrO_2 were 175 Ω, 225 Ω and 50 Ω, respectively[2], demonstrating that the conductivity of ZrO_2 samples showed a positive correlation with the concentration of oxygen vacancies.

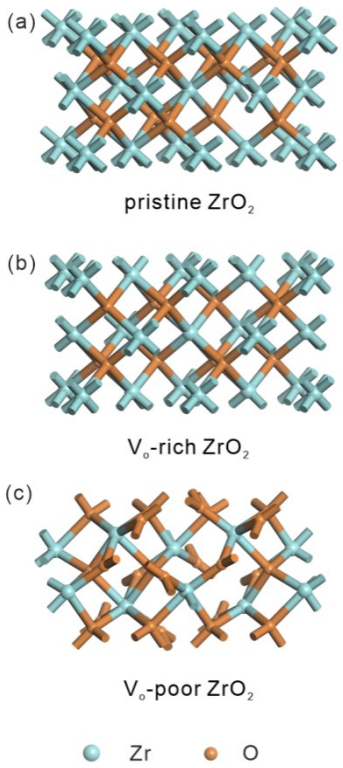

Fig. S8 The optimized structures of (a) pristine ZrO_2; (b) V_o-rich ZrO_2 and (c) V_o-poor ZrO_2.

In optimized structures, tetragonal was used for pristine and V_o-rich ZrO_2, and monoclinic was used for V_o-poor ZrO_2. And the corresponding concentration of the oxygen vacancies in V_o-rich ZrO_2, pristine ZrO_2, and V_o-poor ZrO_2 is 25%, 12.5% and 6.25%, respectively.

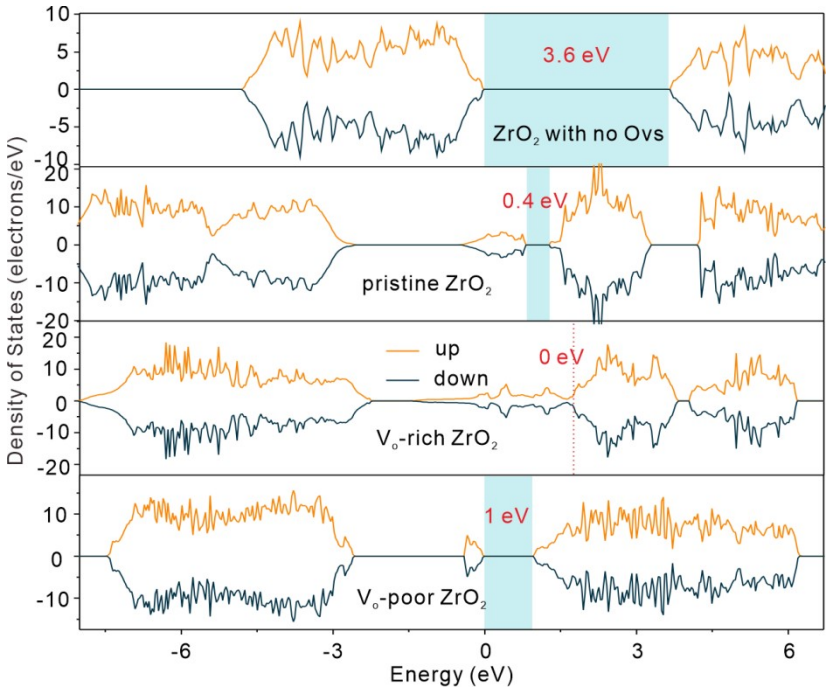

Fig. S9 Comparison of TDOS among pristine ZrO_2, V_o-rich ZrO_2, V_o-poor ZrO_2 and ZrO_2 with no OVs.

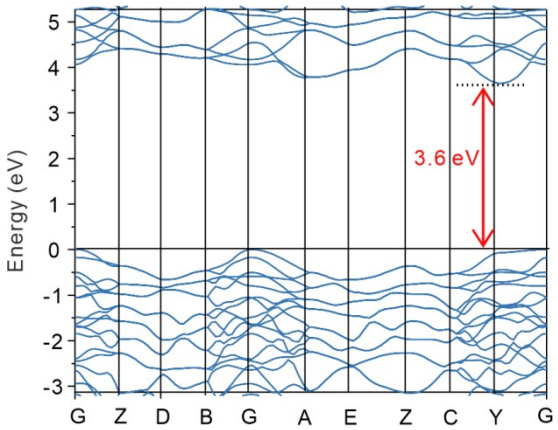

Fig. S10 Band gap diagrams of ZrO_2 with no OVs.

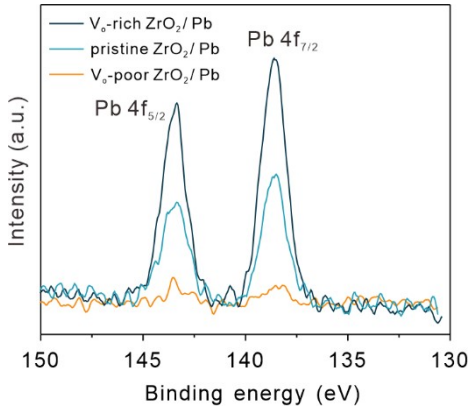

Fig. S11 Comparison of high resolution Pb 4f XPS spectrum among pristine

ZrO_2, V_o-poor ZrO_2, and V_o-rich ZrO_2 after adsorption Pb(II).

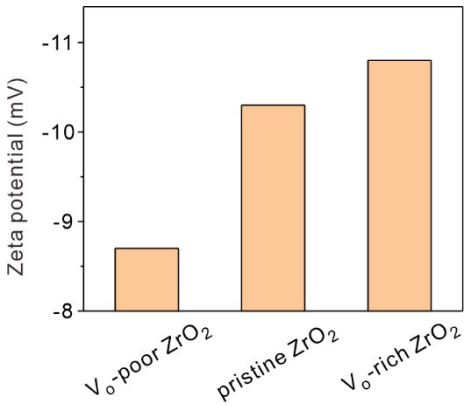

Fig. S12 Zeta potential of three samples in HAc–NaAc buffer solution at pH = 5.

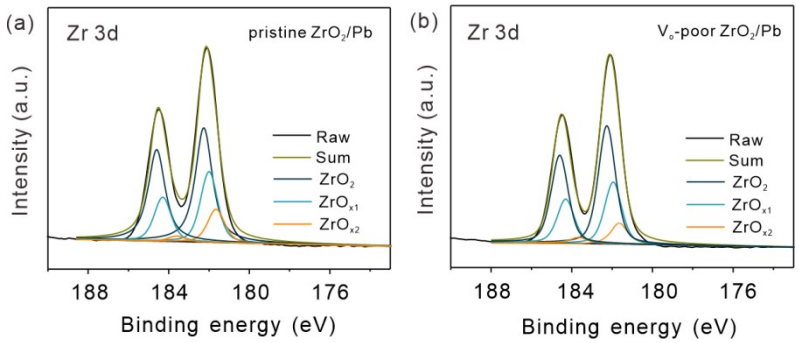

Fig. S13 XPS Zr 3d spectra of (a) pristine ZrO_2/Pb and (b) V_o-poor ZrO_2/Pb.

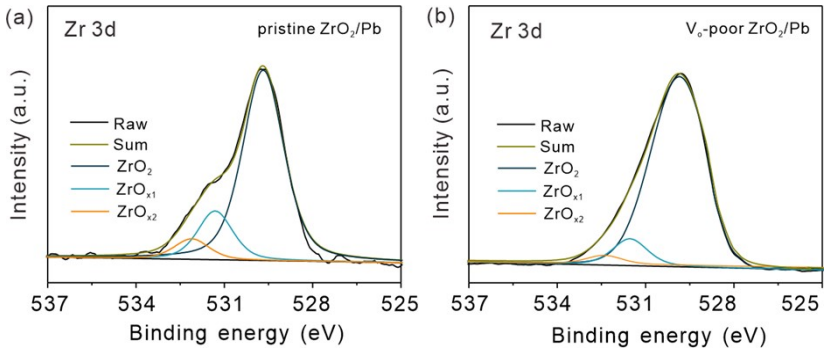

Fig. S14 XPS O 1s spectra of (a) pristine ZrO_2/Pb and (b) V_o-poor ZrO_2/Pb.

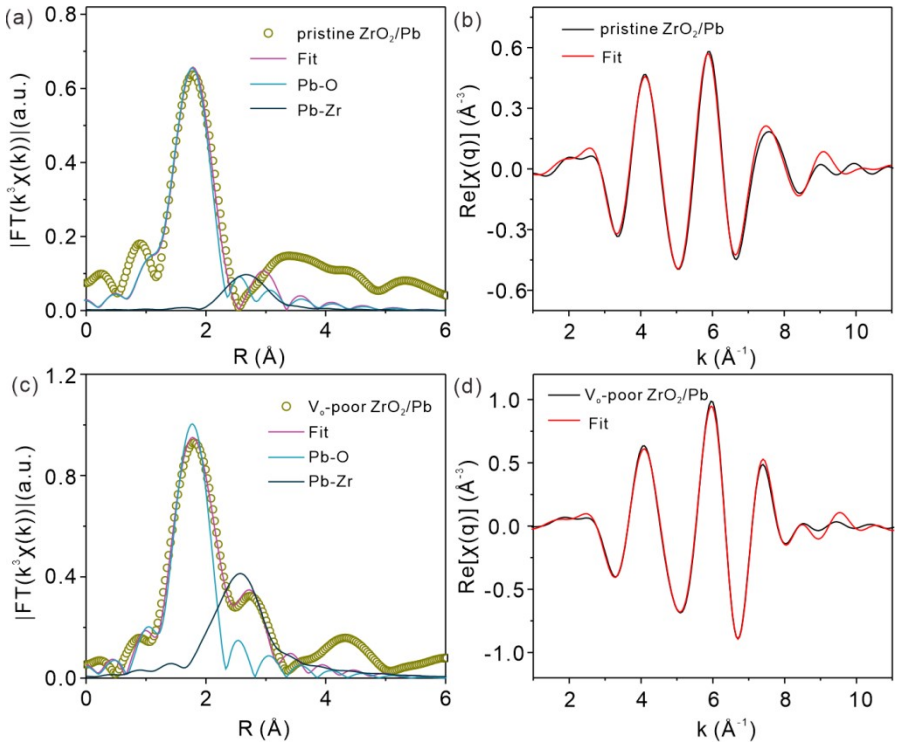

Fig. S15 The Pb L_3-edge EXAFS in R space (k^3-weighted) and the fitting curves of (a) pristine ZrO_2/Pb; (c) V_o-poor ZrO_2/Pb without correcting for scattering phase shift. (b, d) The corresponding k^3(k) oscillations of pristine ZrO_2/Pb; V_o-poor ZrO_2/Pb, respectively.

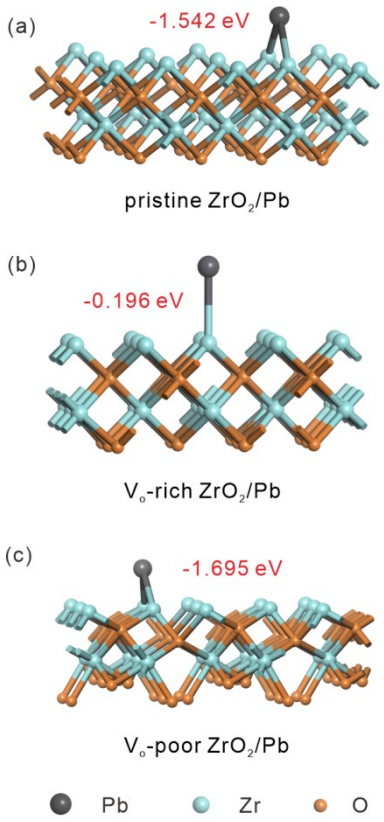

Fig. S16 The optimized configuration after adsorption of Pb(II) on (a) pristine ZrO_2, (b) V_o-rich ZrO_2 and (c) V_o-poor ZrO_2 and the corresponding adsorption energies.

The crystal facet of 010 and the crystal phase of tetragona were used for the adsorption of Pb(II) on V_o-rich ZrO_2 and pristine ZrO_2, where 100 facet, monoclinic phase for that of V_o-poor ZrO_2. During the process of optimization, assuming that the adsorption of Pb(II) occurs directly above Zr atoms, and the adsorption sites of Pb atoms will automatically shift slightly to obtain the present results.

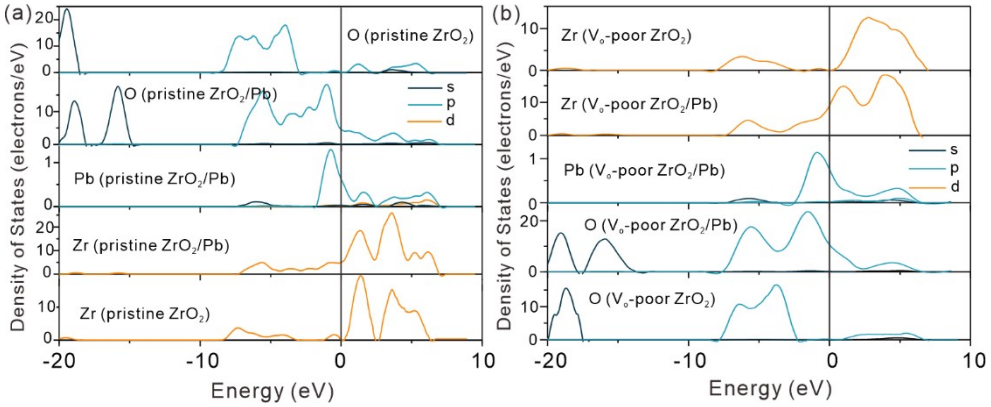

Fig. S17 Comparison of DOS between (a) pristine ZrO_2 and pristine ZrO_2/Pb; (b) V_o-poor ZrO_2 and (c) V_o-poor ZrO_2/Pb.

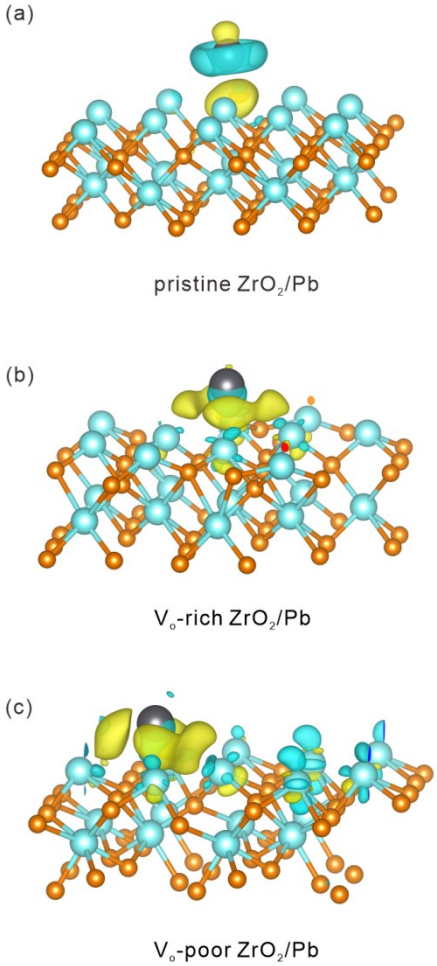

Fig. S18 Charge density difference images of (a) pristine ZrO_2/Pb, (b) V_o-rich ZrO_2/Pb and (c) V_o-poor ZrO_2/Pb. The green areas symbolize electron depletion, and the yellow areas symbolize electron accumulation.

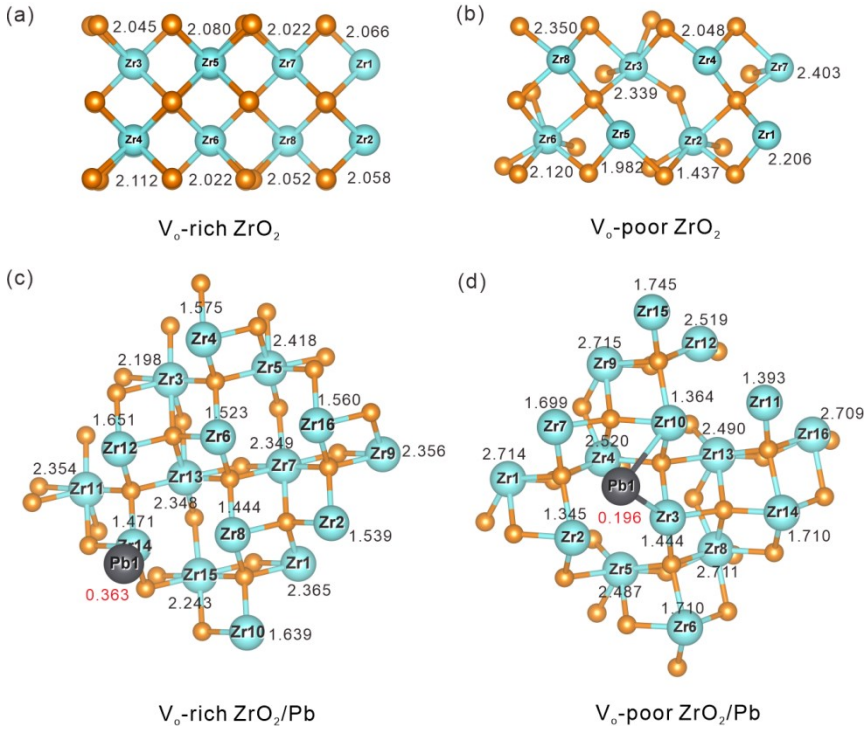

Fig. S19 Absolute value of Bader charge of (a) V_o-rich ZrO_2, (b) V_o-poor ZrO_2, (c) V_o-rich ZrO_2/Pb and (d) V_o-poor ZrO_2/Pb.

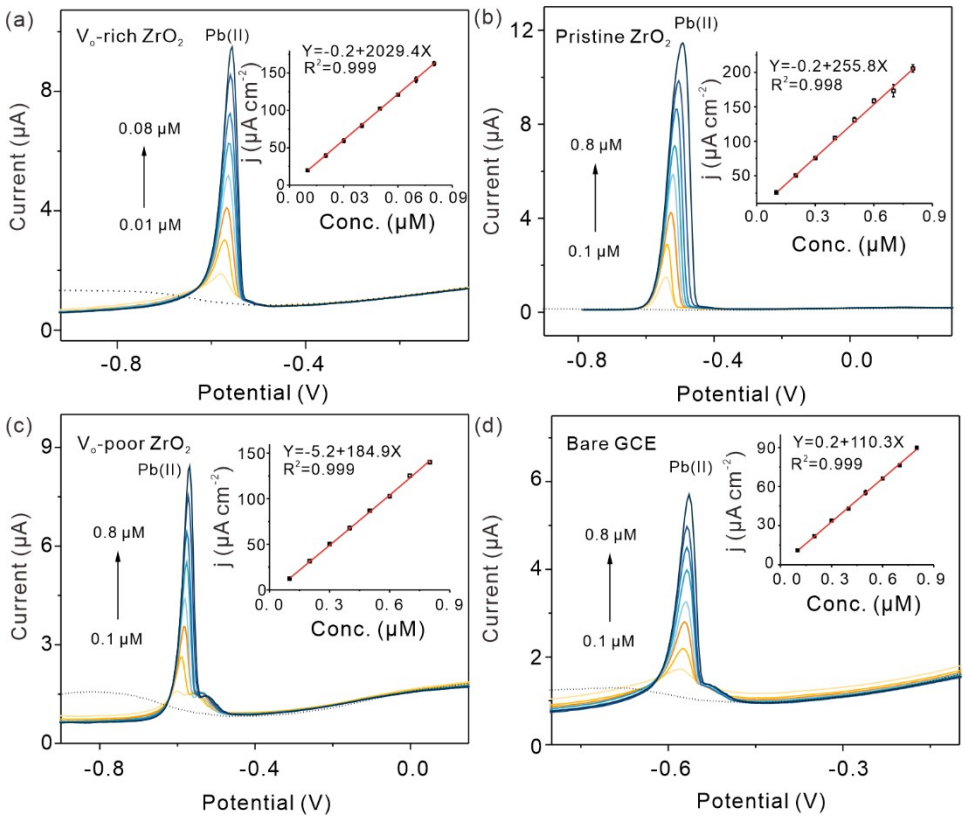

Fig. S20 SWASV responses and linear equations (inset) of Pb(II) on (a) V_o-rich ZrO_2/GCE, (b) pristine ZrO_2/GCE, (c) V_o-poor ZrO_2/GCE, and (d) bare GCE.

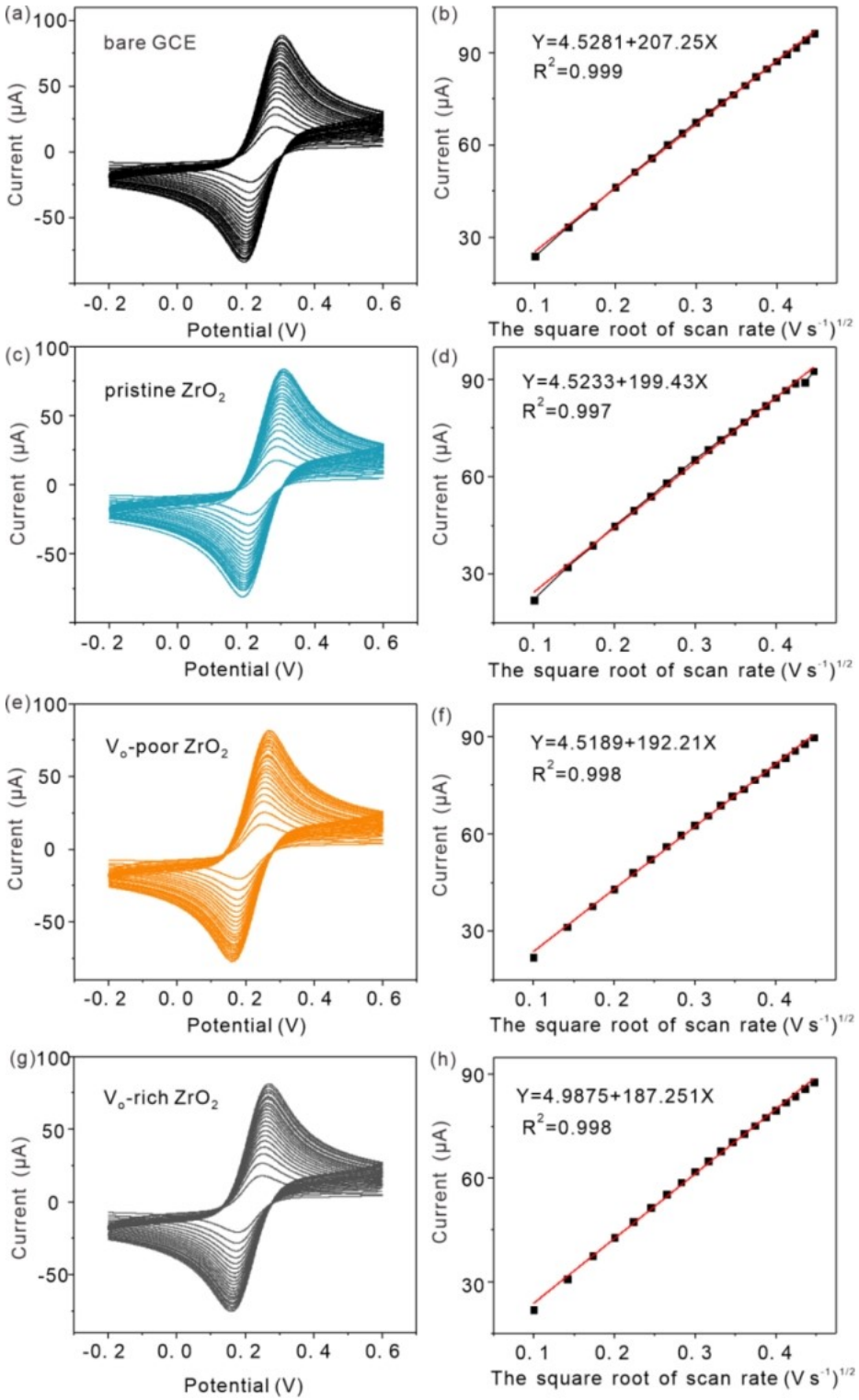

Fig. S21 (a,c,e,g) Scan rate study (from 0.01 to 0.2 V s^{-1}) at bare GCE, pristine ZrO_2,V_o-poor ZrO_2 and V_o-rich ZrO_2, in the solution of 5 mM $Fe(CN)_6^{3-/4-}$ containing 0.1 M KCl, respectively. (b,d,f,h) The corresponding plot of current versus the square root of the scan rate with a linear trend line.

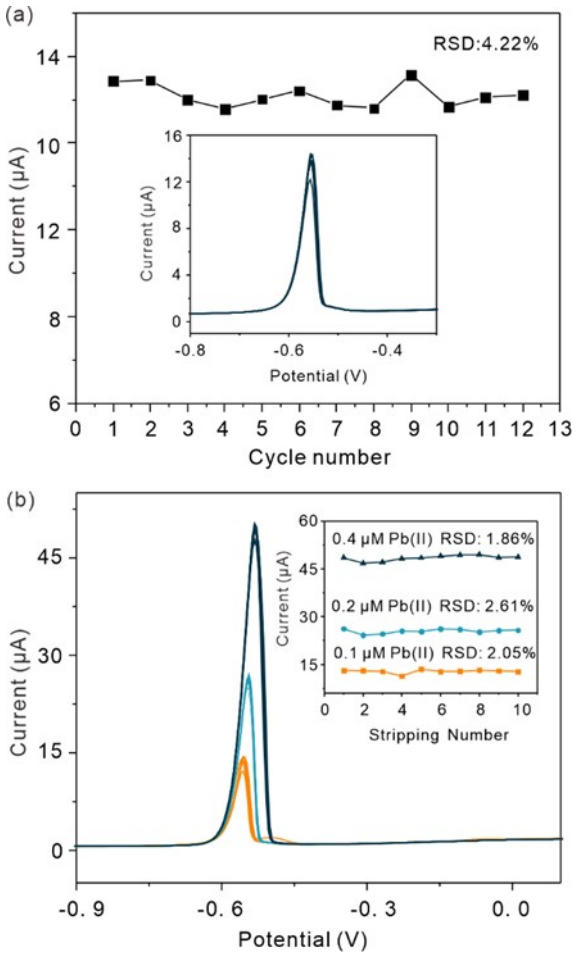

Fig. S22. (a) The stability of V_o-rich ZrO_2/GCE to Pb(II) at the same concentration (0.1 μM). (b) Reproducibility of V_o-rich ZrO_2/GCE at three different concentrations (0.1 μM, 0.2 μM, and 0.4 μM) in the detection of Pb(II).

To evaluate the prospect of practical application of V_o-rich ZrO_2, the corresponding experiments for verifying its catalytic cycle properties have also been carried out. Continuous 13 times SWASV tests of V_o-rich ZrO_2 toward Pb(II) were implemented first with 0.1 μM Pb(II) fixed in HAc-NaAc buffer solution. as shown in Fig. S22a. It can be seen that the relative standard deviation (RSD) of the peak currents of Pb(II) in these thirteen cycles is 4.22% (< 5%), indicating the excellent stability of V_o-rich ZrO_2 during catalytic reaction is obtained. Besides, the peak current signals of ten different GCEs to

be modified with V_o-rich ZrO_2 at three different concentrations (0.1 μM, 0.2 μM, and 0.4 μM) are also examined (Fig. S22b). Similarly, the RSD of these three concentrations are less than 5%, and the RSD of 0.1 μM, 0.2 μM, and 0.4 μM are 2.05%, 2.61%, and 1.86%, respectively, showing excellent reproducibility. These results fully demonstrated that V_o-rich ZrO_2 had excellent catalytic cycle properties, possessing great application prospect in catalysis field.

3. Table

Table S1. Zr K-edge EXAFS fitting results of V_o-rich ZrO_2, pristine ZrO_2 and V_o-poor ZrO_2 samples by the ARTEMIS module of IFEFFIT.

Sample	Path	CN	R(Å)	σ^2 (10^{-3}Å^2)	ΔE_0 (eV)	R-factor	S_0^2
V_o-rich ZrO_2	Zr-O	3.1	2.20±0.01	2.0±0.5	-1.4±0.5	0.006	0.86
	Zr-Zr	7.0	3.46±0.01	7.5±0.4	-7.2±1.0		
pristine ZrO_2	Zr-O	3.6	2.21±0.01	2.8±0.2	-2.0±0.2	0.02	
	Zr-Zr	7.4	3.46±0.02	4.6±0.3	-2.4±2.0		
V_o-poor ZrO_2	Zr-O	3.9	2.22±0.01	1.9±0.2	-4.8±0.7	0.008	
	Zr-Zr	7.6	3.47±0.02	6.8±0.5	-6.4±0.6		

Table S2. The calculated surface energies on {101} and {-111} with different OVs concentration.

Sample	Surface Energies (J/m^2)
{101}-1OV	2.70
{101}-2OV	3.08
{101}-3OV	3.49
{-111}-1OV	1.92
{-111}-2OV	2.60
{-111}-3OV	3.16

Table S3. Defect-related features (ZrO_{x1}, ZrO_{x2}, and their sums) of Zr 3d and O 1s.

	O 1s			Zr 3d		
	ZrO_{x1}	ZrO_{x2}	ZrO_{x1} + ZrO_{x2}	ZrO_{x1}	ZrO_{x2}	ZrO_{x1} + ZrO_{x2}
Pristine ZrO_2	21.17	15.42	36.59	38.86	3.87	42.73
pristine ZrO_2/Pb	16.58	6.99	23.57	27.66	9.78	37.44
V_o-poor ZrO_2	11.95	1.50	13.45	35.70	3.27	38.97
V_o-poor ZrO_2/Pb	9.70	1.35	11.05	15.21	9.85	25.06
V_o-rich ZrO_2	21.98	20.00	41.98	43.09	4.30	47.39
V_o-rich ZrO_2/Pb	14.90	12.75	27.65	31.70	7.74	39.44

Table S4. Pb L_3-edge EXAFS fitting results of V_o-rich ZrO_2/Pb, pristine ZrO_2/Pb and V_o-poor ZrO_2/Pb samples by the ARTEMIS module of IFEFFIT.

Sample	Path	CN	R(Å)	σ^2 (10^{-3}Å^2)	ΔE_0 (eV)	R-factor	S_0^2
V_o-rich ZrO_2/Pb	Pb-O	1.2	2.30±0.01	7.0±0.4	-4.6±0.5	0.002	
	Pb-Zr	1.0	3.04±0.02	5.8±0.4	12.5±1.0		
pristine ZrO_2/Pb	Pb-O	1.3	2.28±0.01	8.4±0.2	-4.4±0.2	0.009	0.80
	Pb-Zr	1.0	3.01±0.02	5.2±0.3	20.5±2.0		
V_o-poor ZrO_2/Pb	Pb-O	1.5	2.29±0.01	7.0±0.2	-2.6±0.7	0.006	
	Pb-Zr	1.2	3.00±0.02	7.9±0.5	17.3±0.6		

Table S5. Bader charge of Zr, O, and Pb calculated by DFT.

Configurations	Bader charge (*e*)		
	Zr	O	Pb
V_o-poor ZrO_2	-2.111	1.126	-
V_o-poor ZrO_2/Pb	-2.080	1.103	0.196
V_o-rich ZrO_2	-2.052	1.368	-
V_o-rich ZrO_2/Pb	-1.396	1.278	0.363

4. Reference

1. L. Zhao, J. Zhao, T. Wu, M. Zhao, W. Yan, Y. Zhang, H. Li, Y. Wang, T. Xiao and Y. Zhao, *Nanomaterials*, 2019, **9**, 406.
2. Y. Y. Li, Z. Y. Song, X. Y. Xiao, L. K. Zhang, H. Q. Huang, W. Q. Liu and X. J. Huang, *J. Hazard Mater.*, 2022, **435**, 129009.